Optimal Design of the PMSM Retaining Plate With 3-D Barrier Structure and Eddy-Current Loss-Reduction Effect

Hyun-Woo Jun, Jong-Wook Lee, Gil-Ho Yoon, and Ju Lee, *Senior Member, IEEE*

***Abstract*—From the constant-speed variable-output motor driving test result of an interior permanent-magnet synchronous motor for a pump drive, we observed that there was an additional loss factor, which was not previously considered. Furthermore, a 3-D finite-element method analysis was performed to investigate the cause of the additional electromagnetic loss. Accordingly, it was confirmed that there was an additional eddy-current loss in the rotor retaining plate structure for the rotor assembly. Using the shape of the eddy-current path in the plate, it was determined that the eddy current was formed inside the plate itself by the bypassing magnetic flux from the permanent magnet and the slot harmonics. It was confirmed that the eddy-current path can be changed according to the structure of the plate, and the optimal retaining plate design that satisfies the design constraints was derived via the topology optimization method. Finally, the retaining plate design with the 3-D barrier structure was derived by arranging the void shape considering the total eddy-current path. Using the actual model test results, it was verified that the new retaining plate design was effective for loss reduction compared to the conventional structure.**

***Index Terms*—Eddy currents, high efficiency, magnetic flux, permanent-magnet motors, slot harmonics, topology optimization, 3-D barrier structure.**

I. Introduction

PERMANENT-MAGNET synchronous motors (PMSMs) are being utilized in various industrial fields owing to their high efficiency [1]. For high-efficiency motor design, it is necessary to design with the consideration of load and driving conditions [2]–[4]. The main design theme and considerations for the motor design of PMSMs in previous studies were related to voltage and current constraints [5], [6], size constraints [7], driving conditions [8], [9], achieving high efficiency and high output density [10]–[12], reducing losses and harmonics [13]–[18], etc. In recent years, many studies related to efficiency improvement and loss reduction of PMSMs have been published. Among the studies on motor losses, the analysis and reduction of eddy-current loss in the rotor are actively studied. According to the classification of the motor winding type, in the concentrated winding type, the eddy-current loss is revealed owing to the inclusion of high harmonics of the air-gap magnetic-flux waveform. Thus, in many papers, studies on the reduction of the eddy-current loss based on the concentrated winding model were performed [18]–[22]. On the other hand, in the case of distributed type motors, the importance of countermeasures against rotor eddy-current losses has been recognized less as compared to the concentrated type motor in the past. Recently, however, many studies on the rotor eddy-current loss in distribution models have been published for loss reduction investigating in order to achieve ultrahigh efficiency [17], [23]–[26]. In a previous study on the loss of the distribution model, the effects of rotor eddy current on slot harmonics and switching harmonics were published [23], and an efficient and reliable eddy-current analysis model was derived using a 3-D finite-element method (FEM) analysis of the PMSM model [24], [25]. It has been demonstrated that the eddy-current loss at the rotor surface and the permanent magnet are of considerable significance during the high-speed operation of interior permanent-magnet synchronous motor (IPMSM) [26], and there have also been discussions on the effect of the eddy-current loss on the conductor of the rotor assembly and the countermeasures to reduce it [17].

In this study, we investigated the loss factor of a region that was not considered in the conventional 2-D FEM analysis by using the 3-D model including the entire rotor assembly. In the conventional 2-D FEM analysis, the permanent magnets are considered insulated from each other by the core. However, in this 3-D model, it was confirmed that the entire eddy-current path was integrated and the loss distribution pattern was different from the previous analysis. The IPMSM type motor introduced in this paper is intended for driving a constant-speed variable-output operation vacuum pump applied to a semiconductor production facility line. The production line drives continuously

Manuscript received December 27, 2016; revised April 17, 2017 and June 4, 2017; accepted June 12, 2017. Date of publication August 7, 2017; date of current version December 8, 2017. This work was supported in part by the Human Resources Program in Energy Technology of the Korea Institute of Energy Technology Evaluation and Planning under Grant 20154030200900 and in part by the National Research Foundation of Korea (NRF) grant funded by the Korea government (MSIP) (No. 2016R1A2A1A05005392). *(Corresponding author: Ju Lee.)*

H.-W. Jun and J. Lee are with the Department of Electrical Engineering, Hanyang University, Seoul 133-791, South Korea (e-mail: jhwinc@hanyang.ac.kr; julee@hanyang.ac.kr).

J.-W. Lee and G.-H. Yoon are with the Department of Mechanical Engineering, Hanyang University, Seoul 133-791, South Korea (e-mail: cleng@hanyang.ac.kr; ghy@hanyang.ac.kr).

Color versions of one or more of the figures in this paper are available online at http://ieeexplore.ieee.org.

Digital Object Identifier 10.1109/TIE.2017.2736501

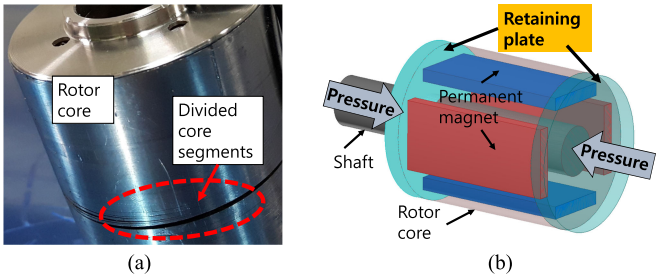

Fig. 1. Rotor core assembly. (a) Divided rotor core segments. (b) PMSM rotor assembly with retaining plate structure.

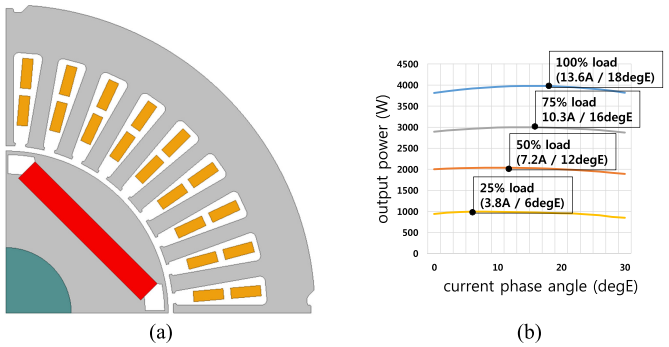

Fig. 2. Design result of 4-kW pump driving motor. (a) 1/4 period model of the motor. (b) Input current and output characteristics according to load.

because it takes a significant amount of time and cost to resume the process when the facility line shuts down [27]. Thus, high-efficiency motor design is important. In this application, the main operating area is located in the light-load range (25%–50% of rated power); hence, the motor design was focused on achieving high efficiency in all the output regions including the light-load area through the consideration of size- and loss-reduction techniques. In the pump design, the impeller with a specific shape has its own maximum efficiency by achieving specific speed, which is a relationship between rotation speed (N), flow rate (Q), and total head (H), regardless of its size [28]. When designing the pump, the design results are obtained according to the required flow rate and pressure using the superposition method with a fixed rotational speed [28]. Therefore, in the case of a pump drive motor, the optimal operating speed is observed to be constant for a specific design value. Therefore, the pump drive motor in this study was designed to change its output while operating at constant speed.

In this study, while confirming the driving characteristic of the pump driving IPMSM motor in variable-output operation, it was observed that there was an unexpected additional no-load loss in the motor. Furthermore, the 3-D FEM analysis indicated that the cause of the additional loss was the eddy-current flow by the bypassing magnetic flux and slot harmonics in the rotor retaining plate structure. In order to reduce the eddy current generation while preserving the structural stiffness of the retaining plate, a design optimization process using the topology optimization design method was carried out. Additionally, the efficiency improvement of the optimized model was verified using the motor dynamo test result and 3-D FEM analysis, which includes a pulse width modulation (PWM) current waveform.

II. Design Parameters and Efficiency Comparison

A. Design Considerations and Parameters of the Vacuum Pump Driving Motor

In electrical machines that use a permanent magnet in the rotor part, the laminated rotor core sheets are subjected to a magnetic force spreading outward. Therefore, in order to prevent the deformation of the rotor core during manufacturing, it requires a structure—such as a panel—for fixing the rotor assembly. Fig. 1 shows a rotor assembly with a fixing panel structure, which holds the rotor core on both the outer sides. The fixing panel structure is called a retaining plate, which allows the rotor core to maintain its shape. Furthermore, it becomes the machining area for balancing the rotor.

In this application, the main operating range is located in the light-load region (less than 50% of the rated load), but stable operation in the full-load area is also required depending on the operating conditions. Therefore, if the size of the motor becomes too small, with the aim of only achieving maximum efficiency in the light-load region, which is the main area of use, there may be excessive heat generation owing to an increase in the current density in the full-load operation region. Therefore, it is necessary to determine the motor size based on the current density, which does not cause a problem in the full-load operation area. Thus, as the core volume increases, the proportion of iron loss becomes relatively higher than the copper loss, compared to the single driving point reference design under light load. Therefore, in this case, an optimum design to reduce the iron loss in the core is necessary to achieve maximum motor efficiency.

Fig. 2 and Table I show the design parameters and current control of the 4-kW vacuum pump IPMSM design according to these design considerations. During the motor control, the maximum efficiency control according to various loads was achieved, and since the proportion of iron loss was higher, the maximum efficiency control trajectory was slightly different from the maximum torque/current curve (MPTA curve) [8].

TABLE I
Design Constraints and Parameters of the Model

Design constraint	Value	Design parameter	Value
Rated power	4 kW	Pole/slot	4/36
Rated speed	6000 r/min	Stator diameter	118 mm
Rated voltage	220 V	Rotor diameter	62 mm
Current density	7 A/mm^2	Stacking length	70 mm
Core material	35PN230	Rated current /phase angle	13.6 A_{rms} /18 degE
Magnet material	NdFeB-N40UH	Efficiency	96.5%

B. Efficiency Comparison of FEM Analysis and Test Result

After the designed model was manufactured, the efficiency at each load point was measured using the motor dynamo test.

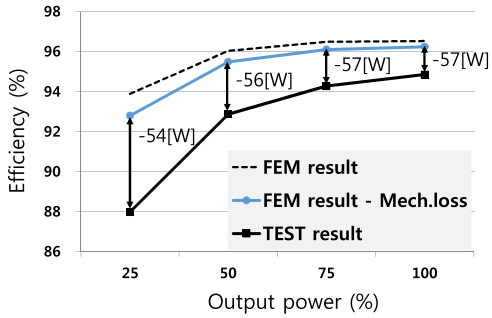

Fig. 3. Comparison between 2-D FEM and test efficiency result.

TABLE II
OUTPUT POWER CORRESPONDING TO EFFICIENCY GAP

Load	Efficiency (Test result/FEM result—Mechanical loss)	Output power corresponding to efficiency gap
25%	87.97%/92.79%	54 W
50%	92.87%/95.48%	56 W
75%	94.27%/96.10%	57 W
100%	94.85%/96.24%	57 W

Subsequently, we compared the difference between the characteristics expected from the 2-D FEM analysis and those obtained from the test result of the actual model. Fig. 3 and Table II compare the 2-D FEM analysis with the efficiency test result of the actual model at the rated speed of 6000 r/min. The results obtained by considering the measured mechanical loss are shown in the graph. The value of pure mechanical loss can be obtained from the dynamo test result using a dummy rotor without permanent magnet [29]. The reason for the lower efficiency in the light-load region is that in the case of constant-speed variable-output, the no-load losses have a relatively constant value even when the output changes, such that the total loss ratio is larger in the light-load region. Comparing the results of FEM analysis with the test results, the efficiency value of the test result was observed to be lower than that of the FEM analysis in all the output regions. It can be observed that almost the same amount of output corresponding to the efficiency gap exists in the entire output region. It can be concluded that this loss has the characteristic of the aforementioned no-load loss. This difference causes the efficiency curve of the actual model test to drop more sharply toward the light load as compared to the efficiency curve of the FEM analysis.

III. ANALYSIS OF ADDITIONAL EDDY-CURRENT LOSS IN THE RETAINING PLATE STRUCTURE

A. Magnetic Field Description and Eddy-Current Distribution

The analytical considerations of magnetic flux density distributions and eddy current density distributions in the rotor eddy-current region have been extensively studied in the existing papers. Furthermore, 2-D FEM presents good eddy-current analysis results for an axially symmetric motor model. However, if the structure is thin or leaky, or if the structure does not appear in the 2-D plane as in the case of this paper, the analysis results obtained can be unreliable. The study in [24] proposed an effective rotor eddy-current model in the distributed PMSM model using the generalized image technique. However, the authors of the aforementioned study assumed that the magnetic flux density distribution in the axial direction is constant, and extended the 2-D FEM field distribution to the 3-D region. In this study, we focus on the formation of the eddy current according to the change of the 3-D field including the retaining plate structure; therefore, the source of x-, y-, and z-components should be introduced. From the Faraday induction law, the distribution of the eddy current density depends on the magnetic flux, which varies with time. When the eddy current density distribution is denoted by J, the flux density B of the 3-D field is decomposed into x-, y-, and z-direction components, and the amount of change with time is denoted as source distribution $S_{x,y,z}$, the relationship between them is as follows [24]:

$$\nabla \times J = \sigma S \tag{1}$$

$$S_x = -\frac{\partial B_x}{\partial t},\ S_y = -\frac{\partial B_y}{\partial t},\ S_z = -\frac{\partial B_z}{\partial t} \tag{2}$$

where σ represents the conductivity of the material. Furthermore, since $\nabla \cdot J = 0$ by conductivity law, J is expressed as the curl of the certain current vector potential A

$$\nabla \times A = J. \tag{3}$$

Using the adopting Coulomb gauge $\nabla \cdot A = 0$, the current vector potential A satisfies the following Poisson equation:

$$\nabla^2 A = -\sigma S. \tag{4}$$

Assuming a conductor in a rectangular parallelepiped area in a rectangular coordinate system, the length of each side is $L_x,\ L_y,\ L_z$. The source distribution $S_{x,y,z}$ including the x-, y-, and z-components is as follows:

$$S_{x,y,z} = \sum_{r=1}^{\infty}\sum_{s=1}^{\infty}\sum_{t=1}^{\infty} a_{x,y,z}\,(r,s,t) \times \cos\left(\Lambda + \theta_{x,y,z}\,(r,s,t)\right) \tag{5}$$

where $\Lambda = r\frac{\pi}{L_x}x + s\frac{\pi}{L_y}y + t\frac{\pi}{L_z}z$.

$S_{x,y,z}$ is obtained through matrix computation for each time step. In 3-D Fourier expansion, $r,\ s,\ t$ represent the harmonic order in each direction; $a_{x,y,z}(r,s,t)$ and $\theta_{x,y,z}(r,s,t)$ represent the magnitude of complex coefficients and phase angle of x-, y-, and z-components, respectively. From (5), the current vector potential satisfying (4) is obtained as follows:

$$A_{x,y,z} = \sum_{r=1}^{\infty}\sum_{s=1}^{\infty}\sum_{t=1}^{\infty} b_{x,y,z}\,(r,s,t) \times \cos\left(\Lambda + \theta_{x,y,z}\,(r,s,t)\right) \tag{6}$$

where $b_{x,y,z}(r,s,t)$ and $\theta_{x,y,z}(r,s,t)$ represent the magnitude of complex coefficients and phase angle of x-, y-, and z-components, respectively.

Consequently, the current density of each component is obtained from aforementioned current vector potential using (3):

$$J_x = \sum_{r=1}^{\infty}\sum_{s=1}^{\infty}\sum_{t=1}^{\infty}\begin{bmatrix} c_{z1}(r,s,t) \times \cos\left(\Lambda + \frac{\pi}{2} + \theta_z(r,s,t)\right) \\ -c_{y1}(r,s,t) \times \cos\left(\Lambda + \frac{\pi}{2} + \theta_y(r,s,t)\right)\end{bmatrix} \tag{7}$$

$$J_y = \sum_{r=1}^{\infty}\sum_{s=1}^{\infty}\sum_{t=1}^{\infty}\begin{bmatrix} c_{x2}(r,s,t) \times \cos\left(\Lambda + \frac{\pi}{2} + \theta_x(r,s,t)\right) \\ -c_{z2}(r,s,t) \times \cos\left(\Lambda + \frac{\pi}{2} + \theta_z(r,s,t)\right)\end{bmatrix} \tag{8}$$

$$J_z = \sum_{r=1}^{\infty}\sum_{s=1}^{\infty}\sum_{t=1}^{\infty}\begin{bmatrix} c_{y3}(r,s,t) \times \cos\left(\Lambda + \frac{\pi}{2} + \theta_y(r,s,t)\right) \\ -c_{x3}(r,s,t) \times \cos\left(\Lambda + \frac{\pi}{2} + \theta_x(r,s,t)\right)\end{bmatrix} \tag{9}$$

where

$$c_{z1} = s\frac{\pi}{L_y}b_z,\quad c_{y1} = t\frac{\pi}{L_z}b_y,$$
$$c_{x2} = t\frac{\pi}{L_z}b_x,\quad c_{z2} = r\frac{\pi}{L_x}b_z,$$
$$c_{y3} = r\frac{\pi}{L_x}b_y,\quad c_{x3} = s\frac{\pi}{L_y}b_x.$$

Furthermore, $c_{x,y,z}(r,s,t)$ and $\theta_{x,y,z}(r,s,t)$ represent the magnitude of complex coefficients and phase angle of x-, y-, and z-components, respectively. Furthermore, $a_{x,y,z}(r,s,t)$, $b_{x,y,z}(r,s,t)$, and $c_{x,y,z}(r,s,t)$ can be obtained from the fast Fourier transform calculation of the original source [25]. From the above equation, the total eddy-current loss of the conductor in the eddy-current region is obtained as follows:

$$P_{\text{eddy}} = \sum_{r=1}^{\infty}\sum_{s=1}^{\infty}\sum_{t=1}^{\infty}\frac{1}{8}\int_0^{L_x}\int_0^{L_y}\int_0^{L_z}\frac{1}{\sigma}\begin{pmatrix} J_{x(r,s,t)}{}^2 \\ +J_{y(r,s,t)}{}^2 \\ +J_{z(r,s,t)}{}^2\end{pmatrix} dxdydz. \tag{10}$$

B. Three-Dimensional FEM Analysis Model Configuration

In this study, we assumed that there is an additional electromagnetic loss, which was not previously considered. Since the plate structure is located outside the laminated core, the retaining plate structure is not included in the 2-D FEM analysis model. In order to identify the cause of the additional electromagnetic loss, a 3-D FEM model was created to confirm the electromagnetic phenomenon in the entire region including the outside of the core. The 3-D FEM model of a 4-kW IPMSM and the material specifications of the analysis model are presented in Table III.

For the calculation of the 3-D FEM analysis model, the material property values of each element are required. The eddy-current analysis region includes a permanent magnet and a retaining plate, whose conductivity is required in addition to permeability. Furthermore, the conductivity of the retaining plate is approximately 2.2 times that of the permanent magnet.

TABLE III
MATERIAL PROPERTIES OF 3-D FEM SIMULATION COMPONENTS

Components	Density	Permeability	Conductivity
Core (35PN230)	7.6 g/cc	(*B*–*H* curve)	–
Magnet (NdFeB-N40UH)	7.4 g/cc	1.10	6.25×10^5 S/m
Retaining plate (STS304)	7.9 g/cc	1.00	1.37×10^6 S/m

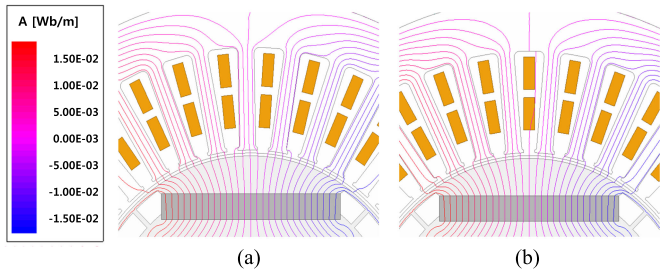

Fig. 4. FEM flux diagram according to the rotor position. (a) Maximum magnetic reluctance position (seven teeth flux path). (b) Minimum magnetic reluctance position (eight teeth flux path).

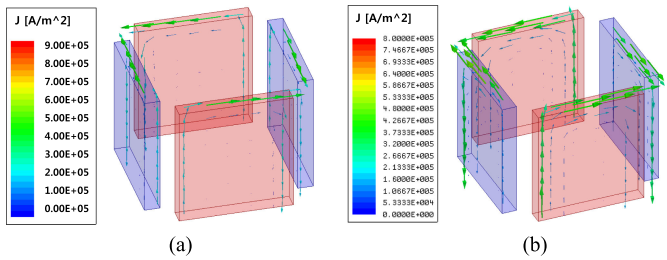

Fig. 5. Periodically changing eddy current flowing through a permanent magnet. (a) Minimum state. (b) Maximum state.

The magnet and plate are in contact with each other to form a conductive path.

C. Analysis Result and Reason for Eddy Current Formation in the Plate Structure

1) Effect of Slot Harmonics on Eddy Current Formation: The flux diagram according to the rotor position between the permanent magnet and the stator during rotation is shown in Fig. 4. In the case of this model, considering the slot opening width and the pole ratio of the permanent magnet, the number of stator teeth that become the magnetic flux path is periodically changed from 7 to 8 during the rotation. In this case, slot harmonics proportional to the number of slots n_s are formed, and a periodic changing eddy current is induced inside the permanent magnet. In the case of an IPMSM, since the magnetic flux bundle passing through the pole piece passes through the permanent magnet, an eddy-current path in the magnet forms a large path over the entire magnet [18]. Owing to the periodicity of change of magnetic reluctance, the magnitude of eddy current changes periodically according to the positional relationship with the slot during rotation as presented in Fig. 5.

2) Effect of the Retaining Plate Structure on the Eddy-Current Path Change: The magnetic flux passes through the

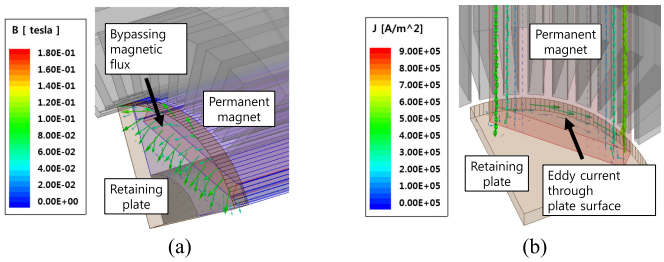

Fig. 6. Bypassing magnetic flux in the plate and eddy current formation in the retaining plate structure. (a) Magnetic flux in the plate structure. (b) Curved eddy-current path in the plate structure.

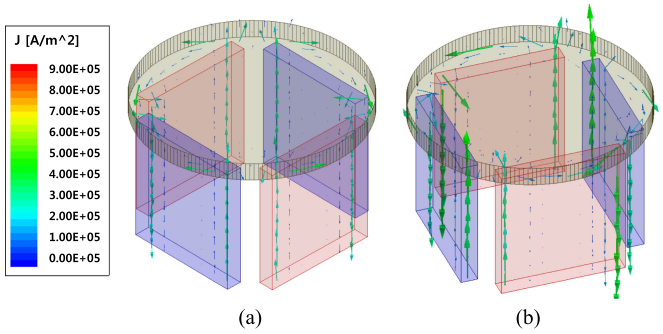

Fig. 7. Periodically changing eddy-current flow through a permanent magnet and plate structure. (a) Minimum state. (b) Maximum state.

plate owing to the bypassing magnetic flux component, and the electromotive force (EMF) is formed on the outer surface of the plate owing to the slot harmonics during rotation as presented in Fig. 6. This phenomenon becomes stronger on the outer surface of the plate, which can be confirmed by the distribution of the eddy-current path through the outer surface of the plate in the 3-D FEM analysis result including the plate structure, as shown in Fig. 6(b). The eddy-current path flow from the magnet to the plate structure does not pass through the shortest way inside the plate but turns to the outer side of the plate; this is the evidence of the fact that the EMF is formed inside the plate itself. Since the eddy current is also caused by the slot harmonics, it has a periodicity depending on its angular position as shown in Fig. 7 similar to the above result. An induced voltage owing to slot harmonics occurs in both the permanent magnet and the plate, and the eddy-current path forms a loop that connects from the permanent magnet to the panel structure.

D. Eddy Current Change According to Shape of Retaining Plate

1) Eddy-Current Characteristic Change According to the Plate Thickness: In order to reduce the eddy-current loss of the retaining plate, we first attempted to observe the effect of eddy current change in the 3-D FEM analysis on the loss characteristic of the actual model. Accordingly, we decided to verify the efficiency improvement effect by changing the thickness of the plate.

When the thickness of the plate changes, the resistance of the plate increases in inverse proportion to the thickness. Consequently, the total resistance of the plate changes, and the magnitude of the total eddy current also changes. When considering the total eddy-current path, the current decreases in inverse proportion to the resistance while the EMF is the same, and the total eddy-current loss also changes because the ohmic loss is obtained as I^2R. The change in the eddy current density in the plate as the thickness of the plate changes is shown in the J magnitude plot of the 3-D FEM analysis below. The generated ohmic loss distribution also follows the same tendency as the current density distribution.

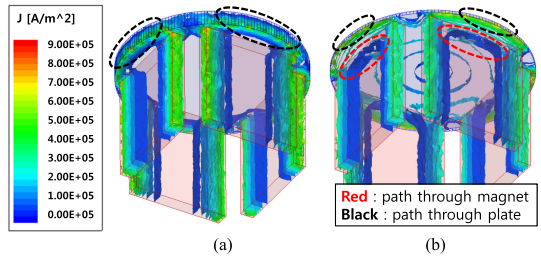

Fig. 8. Comparison of eddy-current distribution change according to the plate thickness. (a) 5-mm plate model. (b) 1-mm plate model.

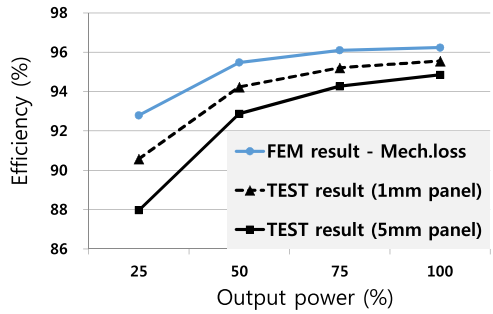

Fig. 9. Test result comparison of motor efficiency characteristic according to the change in plate thickness.

As shown in Fig. 8(a), in the case of a 5-mm plate, the eddy-current flow passes through the outer side of the plate. In the case of a 1-mm plate as shown in Fig. 8(b), the resistance of the plate increases as the thickness of the plate decreases, and the total eddy-current flow from the permanent magnet does not pass through the path in the case of the 5-mm plate, but is partially divided into several paths through the magnet and plate structure. In Fig. 8(b), an eddy-current flow passing through the upper part of the permanent magnet can be observed. This indicates that an eddy current flows through the permanent magnet with a higher resistance, and the magnitude of the total eddy current becomes smaller when the same EMF is applied on the path.

Fig. 9 is a comparison between the efficiency results of the testing model of plates of thickness 5 and 1 mm to see the above analysis results is actually change the output characteristic of the motor. The model used in the test was the same model, and the test results were obtained by replacing the 5-mm plate and the 1-mm plate. The motor driver used in the test was a square-wave inverter among the voltage type inverters. The controller used was the DSP28335 chip and the switching frequency of

TABLE IV
COMPARISON OF NO-LOAD LOSS DYNAMOMETER TEST RESULT

Model	5-mm plate model (prior)	1-mm plate model (tested)
Rotation speed	6000 r/min	6000 r/min
Measured total no-load loss—mechanical loss (test)	116.79 W	86.67 W
No-load core loss (FEM)	57.48 W	
Remaining no-load loss value	59.31 W	29.19 W

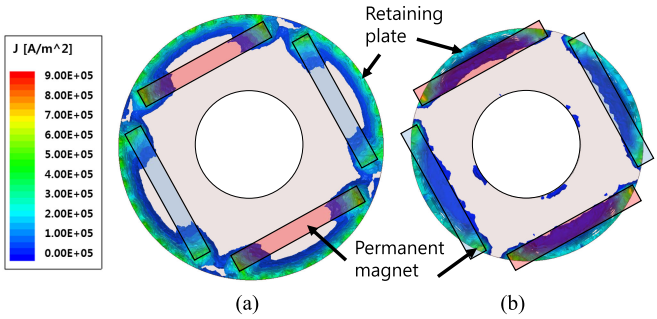

Fig. 10. Comparison of eddy-current distribution on the retaining plate applied to the same core (rotor *D*: 62 mm) according to the change in plate diameter. (a) Eddy-current distribution of (plate *D*: 62 mm). (b) Eddy-current distribution of (plate *D*: 55 mm).

the PWM was 10 kHz. The dead time was 4 μs. As evident from Fig. 9 and Table IV, the efficiency value under the light-load region increases by approximately 2.5% compared to the prior model wherein the 1-mm plate was used. The magnitude of the measured no-load loss was obtained by averaging the two directional measurements of the clock wise and counter clock wise of the dynamo considering the offset of the torque meter. The difference between the no-load loss values of the two models calculated using the difference of the test efficiency values is approximately 30.12 W. Considering the mechanical losses (mainly bearing losses) are almost the same in both results, because they are machining the same motor core and rotating body, we can conclude that the difference between the two test results is caused by the difference in the eddy-current losses of the two plates.

2) Eddy-Current Characteristic Changing According to the Plate Diameter: Further, the change of the eddy-current path and amount of loss owing to the change of the diameter of the plate were confirmed using the 3-D FEM analysis. If the diameter of the plate is changed, the gap between the plate and the stator is changed. Therefore, when the plate becomes smaller, the EMF in the plate owing to the slot harmonics becomes smaller as shown in Fig. 10. Under the same conditions, the smaller the EMF, the smaller the eddy current. The example case used for comparison in Fig. 10(b) is a plate of diameter 55 mm. The result of the smaller plate model demonstrates lighter current density at the outside of the panel as compared to the previous model. However, when the diameter is reduced significantly and if the plate cannot cover the pole piece sufficiently, the plate cannot prevent the deformation of the rotor core by magnetic pressure; therefore, diameter changes have a limited range.

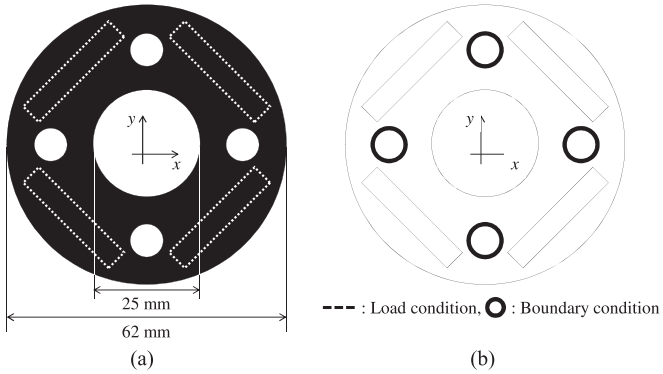

Fig. 11. Design domain and conditions: (a) Design domain of the retaining plate. (b) Boundary condition and force condition of the problem.

IV. OPTIMAL DESIGN OF THE RETAINING PLATE USING THE STRUCTURAL OPTIMIZATION METHOD

A. Structure Optimization—Topology Optimization

As described in Section III-D1, when the resistance of the plate is increased, the current in the entire eddy-current path decreases, and the ohmic loss is reduced. Furthermore, as described in Section III-D2, when the distance between the plate and slot is increased, it is confirmed that the EMF is reduced. However, these structures are not appropriate for actual manufacturing in terms of the structural strength of their original purpose. As evident from the above results, reducing the volume of the plate can increase the total resistance of the plate. Therefore, if we conduct topology optimization with the constraint defined as the volume of the plate structure and the objective function defined as the minimization of the compliance, the resistance of the plate can be maximized while maintaining the required stiffness.

Structural optimization method is a design technique that offers an optimal shape of design according to the objective function and constraints defined by users [30]. Among the structural optimum design techniques, the topology optimization technique is a method that can determine the optimal design by changing the topological information of the design domain [31]–[33]. Since it is possible to form a void in the structure, the method is often used for designing a lightweight structure. In this study, we apply the topology optimization method to obtain an improved shape of the retaining plate with reduced volume. The design domain is set as follows to perform the topology optimization.

The design domain was set to all the parts except the parts connected with bolts in the retaining plate as shown in Fig. 11(a), and the area around the bolt was set to be clamped. The load condition is based on the force from the magnet, and the z-axis load is applied to the dashed line shown in Fig. 11(b). In this study, Young's modulus and Poisson's ratio are set to 190 GPa and 0.3 because the plate is made of stainless steel. The element

used for topology optimization is a quadratic plate element with four nodes and approximately 2600 elements are used.

B. Topology Optimization Formula and Sensitivity Analysis

In this study, the objective function and constraint conditions used to design the retaining plate are as follows:

$$\begin{aligned} \underset{\gamma}{\text{Minimize}} \quad & C = \mathbf{F}^{\mathrm{T}}\mathbf{U} \\ \text{subject to} \quad & V(\gamma) = \sum_{e=1}^{NE} \gamma_e v_e \le V^* \\ & \mathbf{KU} = \mathbf{F} \end{aligned} \tag{11}$$

where

- $\mathbf{F}$ external force vector;
- $\mathbf{U}$ displacement vector;
- $\boldsymbol{\gamma}$ design variable vector;
- γ_e design variable assigned to the eth element;
- v_e volume of the eth element;
- V^* amount of material to be purposed design.

The design variable is called as the "element density" of each element in the design domain. The element density used in the topology optimization technique is a value used to represent the solid or void state of the element and has a value between 0 and 1 [32], [33]. In (11), the objective function (C) is the minimization compliance. The compliance is the mechanical quantity in inverse proportion to the stiffness of the material. Therefore, we can obtain a stiffer structure despite minimizing the compliance [32]. A constraint is defined as the limitation on the amount of material usage. Hence, the optimal design does not exceed the volume fraction and is defined by the designer [32]. Finally, the sensitivity values should be derived because a gradient-based optimizer is used in this study. Generally, the gradient of compliance can be obtained as follows [33]:

$$\begin{aligned} \frac{dC}{d\gamma} &= \frac{d}{d\gamma}\left(\mathbf{F}^{\mathrm{T}}\mathbf{U}\right) = \frac{d\mathbf{F}^{\mathrm{T}}}{d\gamma}\mathbf{U} + \mathbf{F}^{\mathrm{T}}\frac{d\mathbf{U}}{d\gamma} \\ &= \mathbf{F}^{\mathrm{T}}\frac{d\mathbf{U}}{d\gamma} = \mathbf{U}^{\mathrm{T}}\mathbf{K}^{\mathrm{T}}\frac{d\mathbf{U}}{d\gamma} = -\mathbf{U}^{\mathrm{T}}\frac{d\mathbf{K}}{d\gamma}\mathbf{U}. \end{aligned} \tag{12}$$

Based on the above summary, the optimal design topology proceeds as in Fig. 12.

C. Optimization Result

As a result of topology optimization, the final design features were obtained as illustrated in Fig. 13. Fig. 13(a) shows the initial annular plate design with a diameter of 62 mm. Fig. 13(b) shows an optimized design shape when the constraint is limited to 80% of the entire design domain. Notably as presented in Table V, the obtained compliance is increased by 8.83% (stiffness is reduced inversely), which is inevitable because less material is used than in the existing designs.

From the results of the structure optimization, it can be observed that the position of the void shape is approximately near the end of the permanent magnet. Considering the fact that the eddy current is flowing into the panel from the end of the permanent magnet, the void shape was placed in the plate area near the end of the permanent magnet. Thus, the void shape acts as the eddy-current barrier in the 3-D path through the permanent magnet and plate structure to bypass the eddy current.

As a result of examining the structural pattern of the optimum design model, it was confirmed that the void areas increase at both ends of the permanent magnet as the void content increases. As evident from the results of the 3-D FEM analysis, it was confirmed that if there is a barrier in the region, the total eddy-current size can be effectively reduced by bypassing the eddy-current path. In addition, as a result of the examination of the structural strength, it is advantageous that the arrangement of the voids moves to the outer region of the permanent magnet as shown in Fig. 13(c). The overall structure pattern was obtained from the result of Fig. 13(b), but it was adjusted to the proposed

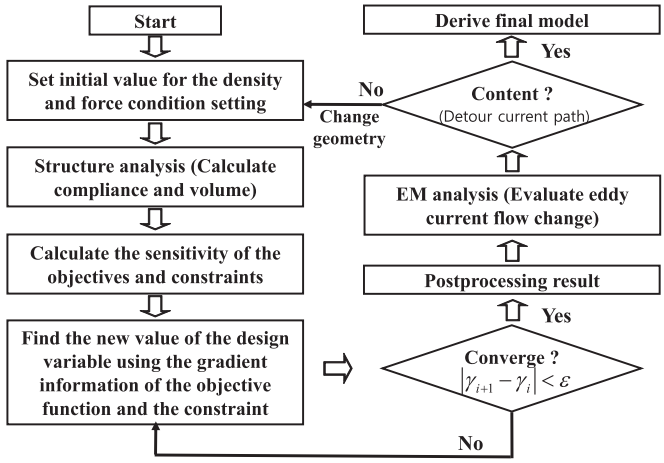

Fig. 12. Topology of the plate design optimization procedure.

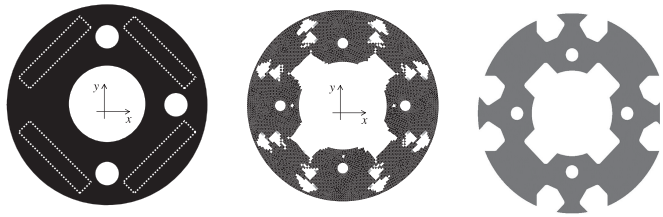

Fig. 13. Topology optimization design results of the retaining plate: (a) Initial design (D: 62 mm), (b) 80% materials used, and (c) final modified design.

TABLE V
COMPARISON OF RESULT OF THE INITIAL DESIGN, OPTIMAL DESIGN, AND THE FINAL MODIFIED DESIGN OF THE STRUCTURE

Model	Volume	Compliance
Initial design (a) (100% material used)	2501.18 mm^3	13.76 mJ
Optimal design (b) (80% material used)	2000.93 mm^3 (20.00% reduced)	14.67 mJ (8.83% increased)
Final design (c) (87.69% material used)	2193.31 mm^3 (12.31% reduced)	14.62 mJ (6.24% increased)

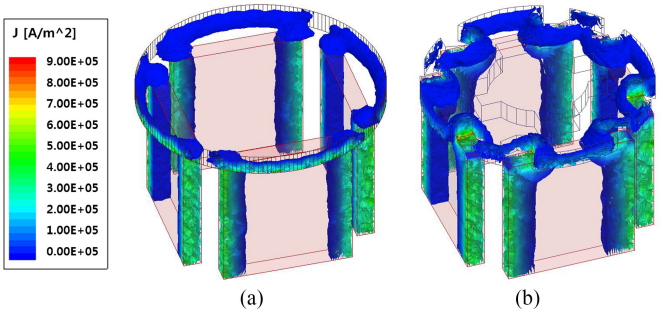

Fig. 14. Comparison of eddy-current generation characteristic of the prior model and proposed model. (a) Prior model. (b) Proposed model.

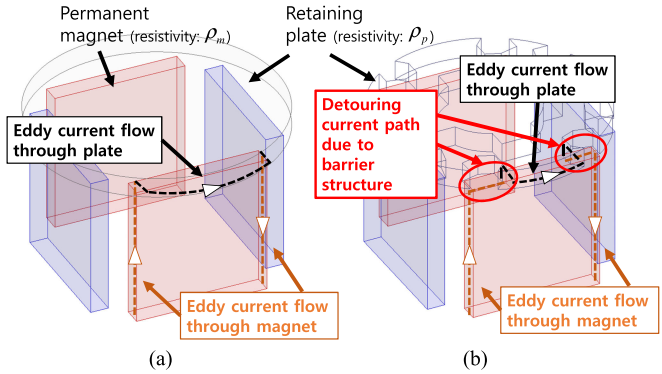

Fig. 15. Comparison of eddy-current flow in the prior model and proposed model. (a) Prior model flow path. (b) Proposed model flow path.

model shape of Fig. 13(c) in order to improve the structural strength, electromagnetic barrier performance, and fabrication.

For the design of model (c), the optimal diameter and thickness of the plate were chosen among the results that satisfied the aforementioned objective function and design constraint conditions. The final design was reevaluated for the structural characteristics. Consequently, it was determined that a diameter of 58 mm and a thickness of 6.5 mm were optimal. Finally, compared to the previous model shown in Fig. 13(a), a final design with approximately 12.31% less material was obtained. Moreover, the compliance has increased by approximately 6.24 %; however, considering the volume reduction, it was considered a reasonable result.

V. Characteristics of the Proposed Design Model and Test Results

A. Loss-Reduction Effect of the Proposed Model

The proposed design results were compared to the previous model in terms of the eddy-current generation characteristic. The compared model is a standard plate model with an initial plate design of a diameter of 62 mm and a thickness of 5 mm.

The prior model has an eddy-current flow path, which includes the outer part of the panel, as shown in Fig. 14(a). However, as shown in Fig. 14(b), the optimal model changes the eddy-current path owing to the arrangement of the 3-D barrier structure inside the panel. The difference in the eddy-current flow between the prior and proposed models is presented in Fig. 15. Owing to the position of the barrier, the eddy current flows through the upper part of the permanent magnet in some sections. As shown in Fig. 15(b), the current path through the magnet with a higher resistance becomes longer than that of the previous model, thus the total resistance increases. If the other design conditions, including the magnitude of the slot harmonics, are the same, the increased resistance in the current path generates smaller size of the total eddy current

$$\begin{aligned}\text{prior model } R_{\text{current path}} \text{ ratio} &: \rho_m L + \rho_p (T + r\theta) + R_{\text{cont}} \\ \text{optimal model } R_{\text{current path}} \text{ ratio} &: \rho_m (L + W \cdot W_B) \\ &+ \rho_p \left(2T + \theta_B \left(r \cos\frac{\theta}{2} \Big/ \cos\frac{\theta_B}{2}\right)\right) + R_{\text{cont}}. \end{aligned} \tag{13}$$

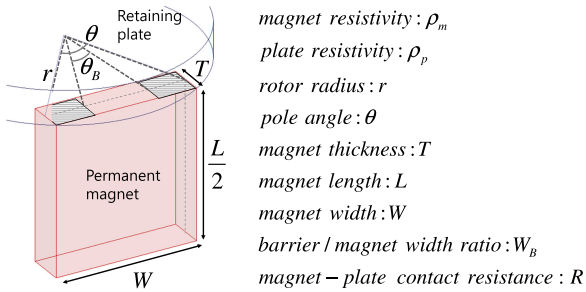

Fig. 16. Design parameters of the region near the eddy-current path.

The main design parameters are presented in Fig. 16 and it shows the positional relationships of the magnet and plate structure schematically. Fig. 16 shows the half-length rotor with the retaining plate model in which the width, length, and thickness of the permanent magnet are W, L, and T, respectively. The shaded area on top of the permanent magnet is the part where the 3-D barrier exists inside the retaining plate. In the case of the proposed model, the eddy current cannot pass through the shaded part as shown in Fig. 14(b):

$$R_{\text{cont}} : (\rho_m + \rho_p)\left(\frac{1}{4na} + \alpha^{-1}\right)$$

where

n number of contacting asperties;

a average radius of contacting asperties. (14)

Equation (14) is a generalized expression of the contact electrical resistance per unit area between the two conductors [34]. It is difficult to determine the exact value because the variables n and a contain variables for temperature and contact pressure, but it is useful to determine the expected range of contact resistance based on the facts discovered in previous studies and certain assumptions. The range of contact resistance between the magnet and the optimal design panel obtained by applying the material properties and shape parameters is $4.55\text{E}-4\,\Omega/\text{m} < R_{\text{cont}} < 6.38\text{E-}3\,\Omega/\text{m}$, and it can be applied to (13). Assuming that the air-gap permeance is the same, the

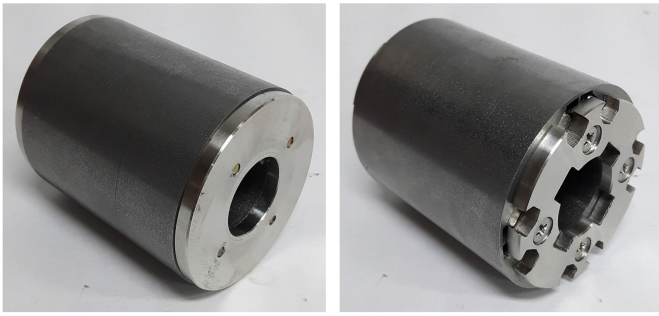

(a) (b)

Fig. 17. Rotor assembly of the manufactured model. (a) Prior model. (b) Proposed model.

TABLE VI
PROPOSED MODEL TEST RESULTS ACCORDING TO OUTPUT REGION

Output Power	25%	50%	75%	100%
Rotation speed (r/min)		6000		
Output power (kW)	1.06	2.06	3.00	4.04
Input current (A)	3.97	7.26	10.34	13.7
Current phase angle (degE)	5	10	15	15
Efficiency (%)	90.6	94.4	95.3	95.7
Power factor	0.98	0.97	0.97	0.95

ratio of magnitude of the eddy-current loss of the proposed model calculated using the above method is distributed at a ratio of at least 0.78 to a maximum of 0.84 times as compared to the conventional method.

B. Verification of Output Characteristics of the Proposed Model

The proposed design model was manufactured and tested to verify its effectiveness. Two types of rotor assemblies were manufactured as shown in Fig. 17. The previous model is shown in Fig. 17(a) and the proposed design model is newly manufactured as shown in Fig. 17(b). The retaining plate was fabricated to be bolted to the rotor assembly. The plate and bolt are made of stainless steel. The rotor assembly of Fig. 17 is coupled to the shaft with lock nuts. Table VI shows the test characteristic results according to the output region of the proposed model. The current magnitude and phase angle that produce the maximum efficiency were controlled while changing the output at the same operating speed. The current phase angle was adjusted by 5 degE. The operating efficiency characteristics according to the output region are shown in Fig. 18. The characteristics of the proposed design model are compared with the efficiency characteristics of the prior model. As evident from the results, an efficiency improvement of approximately 2.5% under light load was achieved.

For the analysis of the loss-reduction effect achieved by the panel change as shown in Fig. 18, the magnitude of the estimated loss from the test result and the calculated loss from FEM were compared. From the test results, the sum of the iron loss and the

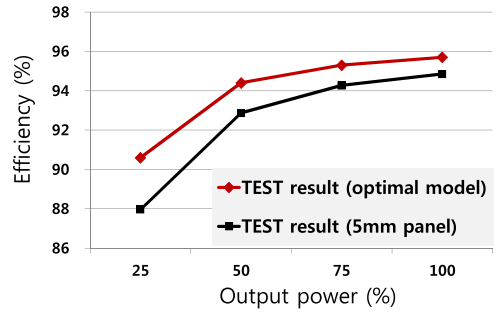

Fig. 18. Comparison of efficiency characteristic of the proposed model according to output power region.

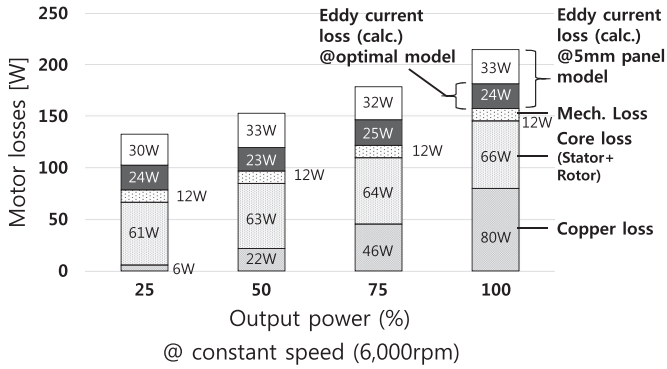

Fig. 19. Comparison of loss ratio according to output region.

eddy-current loss is obtained as follows:

$$P_{\text{core}+\text{eddy}} = P_{\text{in}} - P_{\text{copper}} - P_{\text{mechanical}} - P_{\text{out}}. \tag{15}$$

After replacing the plate part, the predicted eddy-current loss values in each output region from the test results are shown in Fig. 19. The copper losses were calculated using input current and phase resistance. The mechanical losses during rotation were measured using the aforementioned dummy rotor test. The iron losses can be calculated from the magnetic flux density from FEM and the inherent core loss data. The expected eddy-current loss value is the calculated total loss excluding copper loss, core loss, and mechanical loss. It was observed in a test at constant speed operation that the estimated eddy-current loss is approximately 57 W in the conventional model over the entire area and approximately 24 W in the proposed model.

Fig. 20 shows the 3-D FEM model composed of an open circuit and the applied current waveform to confirm the magnitude of the eddy-current loss during the load in the final model. The current waveform during the actual test shown in Fig. 20(b) was applied to each phase. The current was sampled considering the analysis time step from the current waveform data at 4-kW output. The time step of the analysis model is 2.78E-05 s. The analysis results were obtained with a loss of 26.06 W at 4.09-kW output. This result is almost equal to the predicted eddy-current loss, and it is concluded that the resulting difference is due to the error in the analysis model and the selection error of the current data sample.

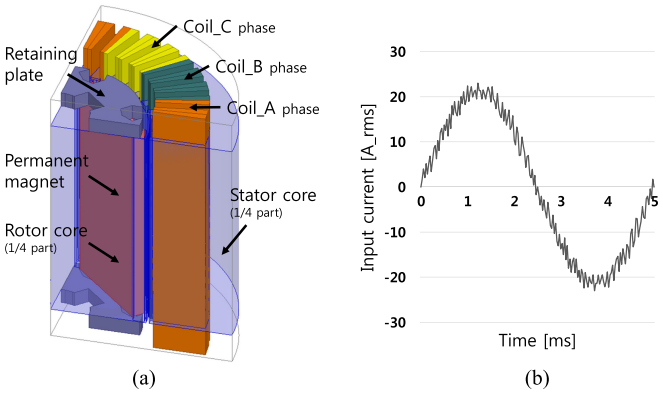

Fig. 20. (a) 1/4 periodic 3-D FEM model of the proposed model. (b) Applied PWM current waveform in the analyzed output region.

VI. Conclusion

In this study, the cause of the eddy-current loss in the rotor retaining plate of an IPMSM was investigated, a 3-D barrier structure inside the retaining plate was derived using the result obtained from the topology optimization technique, and the loss-reduction effect was analytically and experimentally analyzed. It is confirmed that there is an optimum design point that can change the path of the eddy-current flow, and, consequently, minimize the total ohmic loss. Additionally, the prediction of accurate loss amounts in complex geometry using effective eddy-current analysis techniques will be studied in further research.

References

[1] T. J. E. Miller, *Design of Brushless Permanent-Magnet Machines*, 2nd ed. Venice, FL, USA: Motor Design Books LLC, Mar. 2010.

[2] G. Lei *et al.*, "System-level design optimization methods for electrical drive systems: Deterministic approach," *IEEE Trans. Ind. Electron.*, vol. 61, no. 12, pp. 6591–6602, Dec. 2014.

[3] G. Y. Sizov, D. M. Ionel, and N. A. O. Demerdash, "Modeling and parametric design of permanent-magnet AC machines using computationally efficient finite-element analysis," *IEEE Trans. Ind. Electron.*, vol. 59, no. 6, pp. 2403–2413, Jun. 2012.

[4] E. B. Agamloh and A. S. Nagorny, "An overview of efficiency and loss characterization of fractional horsepower motors," *IEEE Trans. Ind. Electron.*, vol. 60, no. 8, pp. 3072–3080, Aug. 2013.

[5] S. Jung, C. Mi, and K. Nam, "Torque control of IPMSM in the field-weakening region with improved DC-link voltage utilization," *IEEE Trans. Ind. Electron.*, vol. 62, no. 6, pp. 3380–3387, Jun. 2015.

[6] Y. W. Li, N. R. Zargari, and B. Wu, "DC-link current minimization for high-power current source motor drives," *IEEE Trans. Power. Electron.*, vol. 24, no. 1, pp. 232–240, Jan. 2009.

[7] T. A. Minav *et al.*, "Permanent magnet synchronous machine sizing: Effect on the energy efficiency of an electro-hydraulic forklift," *IEEE Trans. Ind. Electron.*, vol. 59, no. 6, pp. 2466–2474, Jun. 2012.

[8] R. Antonello, M. Carraro, and M. Zigliotto, "Maximum-torque-per-ampere operation of anisotropic synchronous permanent-magnet motors based on extremum seeking control," *IEEE Trans. Ind. Electron.*, vol. 61, no. 9, pp. 5086–5093, Sep. 2014.

[9] J. Du, X. Wang, and H. Lv, "Optimization of magnet shape based on efficiency map of IPMSM for EVs," *IEEE Trans. Appl. Supercond.*, vol. 26, no. 7, Oct. 2016, Art. no. 0609807.

[10] A. M. EL-Refaie *et al.*, "Advanced high-power-density interior permanent magnet motor for traction applications," *IEEE Trans. Ind. Appl.*, vol. 50, no. 5, pp. 3235–3248, Sep./Oct. 2014.

[11] J. H. Lee and B. I. Kwon, "Optimal rotor shape design of a concentrated flux IPM-type motor for improving efficiency and operation range," *IEEE Trans. Magn.*, vol. 49, no. 5, pp. 2205–2208, May 2013.

[12] X. Lu *et al.*, "Development of a novel magnetic circuit model for design of premium efficiency three-phase line start permanent magnet machines with improved starting performance," *IEEE Trans. Magn.*, vol. 49, no. 7, pp. 3965–3968, Jul. 2013.

[13] J. Hur *et al.*, "Vibration reduction of IPM-type BLDC motor using negative third harmonic elimination method of air-gap flux density," *IEEE Trans. Ind. Appl.*, vol. 47, no. 3, pp. 1300–1309, May/Jun. 2011.

[14] Y. U. Park, J. H. Cho, and D. K. Kim, "Cogging torque reduction of single-phase brushless DC motor with a tapered air-gap using optimizing notch size and position," *IEEE Trans. Ind. Appl.*, vol. 51, no. 6, pp. 4455–4463, Nov./Dec. 2015.

[15] H. K. Samitha Ransara and U. K. Madawala, "A torque ripple compensation technique for a low-cost brushless DC motor drive," *IEEE Trans. Ind. Electron.*, vol. 62, no. 10, pp. 6171–6182, Oct. 2015.

[16] N. Bianchi, M. Degano, and E. Fornasiero, "Sensitivity analysis of torque ripple reduction of synchronous reluctance and interior PM motors," *IEEE Trans. Ind. Appl.*, vol. 51, no. 1, pp. 187–195, Jan./Feb. 2015.

[17] Y. Liang *et al.*, "Finite-element evaluation and eddy-current loss decrease in stator end metallic parts of a large double-canned induction motor," *IEEE Trans. Ind. Electron.*, vol. 62, no. 11, pp. 6779–6785, Nov. 2015.

[18] K. Yamazaki and Y. Fukushima, "Effect of eddy-current loss reduction by magnet segmentation in synchronous motors with concentrated windings," *IEEE Trans. Ind. Appl.*, vol. 47, no. 2, pp. 779–788, Mar./Apr. 2015.

[19] N. Bianchi, D. Durello, and A. Fasolo, "Relationship between rotor losses and size of permanent magnet machines," *IEEE Trans. Ind. Appl.*, vol. 49, no. 5, pp. 2015–2023, Sep./Oct. 2015.

[20] J. Blum *et al.*, "Modeling and reduction of stator teeth eddy current losses in IPM machines," in *Proc. Int. Conf. Electr. Mach.*, Sep. 2014, pp. 1300–1306.

[21] T. Okitsh *et al.*, "Coupled 2D and 3D eddy current analysis for evaluating eddy current loss of a permanent magnet in surface PM motors," *IEEE Trans. Magn.*, vol. 48, no. 11, pp. 3100–3103, Nov. 2012.

[22] Y. Yoshida, K. Nakamura, and O. Ichinokura, "Consideration of eddy current loss in SPM motor based on electric and magnetic networks," *IEEE Trans. Magn.*, vol. 48, no. 11, pp. 3108–3111, Nov. 2012.

[23] K. Yamazaki and A. Abe, "Loss investigation of interior permanent magnet motors considering carrier harmonics and magnet eddy currents," *IEEE Trans. Ind. Appl.*, vol. 45, no. 2, pp. 659–665, Mar./Apr. 2009.

[24] L. Chen, J. Wang, and S. S. Nair, "An analytical method for predicting 3D eddy current loss in permanent magnet machines based on generalized image theory," *IEEE Trans. Magn.*, vol. 52, no. 6, Jun. 2016, Art. no. 8103311.

[25] S. S. Nair *et al.*, "Computationally efficient 3D rotor eddy current loss prediction in permanent magnet machines," in *Proc. Int. Conf. Electr. Mach.*, Sep. 2016, pp. 1426–1432.

[26] J. Yon *et al.*, "Analysis of semipermeable contaminent sleeve technology for high speed permanent magnet machines," *IEEE Trans. Energy Convers.*, vol. 27, no. 3, pp. 646–653, Sep. 2012.

[27] K. C. Lee *et al.*, "Electric monorail system with magnetic levitations and linear induction motors for contactless delivery applications," in *Proc. IEEE 8th Int. Conf. Power Electron. ECCE Asia*, South Korea, May 30, 2015, pp. 2462–2465.

[28] G. E. Totten, *Handbook of Hydraulic Fluid Technology*, 2nd ed. Boca Raton, FL, USA: CRC Press, 2012.

[29] P. D. Pfister and Y. Perriard, "Very-high speed slotless permanent-magnet motors: Analytical modeling, optimization, design and torque measurement methods," *IEEE Trans. Ind. Electron.*, vol. 57, no. 1, pp. 296–303, Jan. 2010.

[30] J. Arora, *Introduction to Optimum Design*. San Francisco, CA, USA: Academic, 2004.

[31] K. Suzuki and N. Kikuchi, "A homogenization method for shape and topology optimization," *Comput. Methods Appl. Mech. Eng.*, vol. 93, pp. 291–318, 1991.

[32] B. M. Philip and O. Sigmund, *Topology Optimization: Theory, Methods, and Applications*. New York, NY, USA: Springer Science and Business Media, 2013.

[33] O. Sigmund, "A 99 line topology optimization code written in MATLAB," *Struct. Multidiscip. Optim.*, vol. 21, pp. 120–127, 2001.

[34] M. Vogler and S. Sheppard, "Electrical contact resistance under high loads and elevated temperatures," *Welding* , pp. 231–238, Jun. 1993.

Hyun-Woo Jun received the B.S. and M.S. degrees in electrical engineering from Hanyang University, Seoul, South Korea, in 2012 and 2014, respectively, where he is currently working toward the Ph.D. degree in new design technique development of high efficiency and power density synchronous motors.

His main research interests include electric machinery and drives, electromagnetic design of motor and generator, and applications of mechatronics systems in robotics, automotive parts, and electric vehicles.

Jong-Wook Lee received the B.S. degree in mechanical engineering from Kyungpook National University, Daegu, South Korea, in 2010. Since 2013, he s currently working toward the Ph.D. degree in new structural optimization methods to design lightweight structures that can prevent structural failure.

His research interests include structural and multidisciplinary optimization, topology optimization, static failure, and dynamic failure.

Gil-Ho Yoon received the M.S. and Ph.D. degree degrees in mechanical engineering from Seoul national University, Seoul, South Korea.

In 2011, he joined Hanyang University, Seoul, where he is currently a Professor in the Division of Mechanical Engineering. His main research interests include structural and multidisciplinary optimization, topology optimization, and fluid structure interaction.

Ju Lee (SM'15) received the M.S. degree in electrical engineering from Hanyang University, Seoul, South Korea, in 1988, and the Ph.D. degree in electrical engineering from Kyusyu University, Fukuoka, Japan, in 1997.

In September 1997, he joined Hanyang University, where he is currently a Professor in the Division of Electrical and Biomedical Engineering. His main research interests include electric machinery and drives, electromagnetic field analysis, and transportation systems, such as hybrid electric vehicles and high-speed electric trains.

Dr. Lee is a member of the IEEE Industry Applications Society, the Magnetics Society, and the Power Electronics Society.